Available online at www.easd.procedia.org
EASD Procedia EURODYN (2026) 1325-1342

EASD Procedia

EURODYN 2026
XIII International Conference on Structural Dynamics
M. Beer, C. Papadimitriou, H. Jensen, J. Chen, M. Broggi, J. Behrensdorf (eds.)
Hannover, Germany, 27.09.–01.10 2026

A COMPARATIVE ANALYSIS OF THE DYNAMIC PERFORMANCE OF BALLASTED AND BALLASTLESS TRACK SYSTEMS FOR HIGH-SPEED TURNOUTS

L. Faccini[1], L. Bernardini[1], E. Di Gialleonardo[1], C. Somaschini[1], A. Collina[1] and G. Diana[1]

[1] Department of Mechanical Engineering, Politecnico di Milano
Via G. La Masa 1, Milano, 20156
e-mail: leonardo.faccini@polimi.it

Keywords: High-speed turnouts, Switches, Slab track, Ballasted track, Train-track interaction.

Abstract. *Railway infrastructure plays a fundamental role in enabling the daily movement of people and goods. In a context characterised by higher dynamic loads, speeds, and traffic demand, it is essential to continuously ensure safety and operability of the network and its subcomponents. Among these, turnouts are particularly critical systems due to their geometric complexity, the high maintenance costs involved and their function. Because of the geometry of wheel–rail contact and the abrupt variations of track flexibility, severe impact loads are generated during train crossing. These loads can significantly damage the turnout and accelerate the degradation of the supporting track substructure, compromising the safety functioning of the system. In this work, a preliminary comparative analysis is conducted considering, respectively, turnouts laid on conventional ballasted and ballastless layers. To this end, a detailed finite element model of a high-speed movable-point turnout has been developed, accounting for the variability of rail profile along the longitudinal direction. The dynamic interaction between the trainset, modelled through a multi-body approach, and the turnout structure is simulated using a non-commercial software developed inside the Department of Mechanical Engineering at Politecnico di Milano. Train-track coupling is realised through wheel-rail contact forces, defined using a multi-Hertzian approach that can reproduce the formation of multiple contacts between each wheel and the different rails. The two track options are compared in terms of track accelerations as well as dynamic forces transmitted to the ground. For the turnout sections considered and under the simulation parameters adopted, sleeper midspan acceleration levels were found to be higher for the slab track configuration. Nevertheless, this solution provides a more uniform distribution of the forces transmitted to the ground, thereby reducing their peak values.*

ISSN:2311-9020 © 2026 The Authors. Published by EASD Procedia.
Peer-review under responsibility of the Organizing Committee of EURODYN 2026.
doi: 10.47964/1326.10744.341

1 INTRODUCTION

Railway networks, whose continuous availability is fundamental for social activities and economic growth, represent a pillar of land transportation infrastructure and play a central role in the development of sustainable transport systems [1]. Growing speeds, loads [2] and traffic density [3] enhance and accelerate the degradation of infrastructure components. Among these, turnouts are complex and critical systems, characterised by severe dynamic interaction with running vehicles [4–7]. Precisely, the rapid variations of wheel-rail contact geometry lead to large dynamic contact forces that can cause wear, accumulated plastic deformation and rolling contact fatigue [8]. The dynamic interaction with travelling trains may cause severe degradation of switch panels as well as of the underlying ballast and subgrade layers. Ballast degradation, in turn, produces differential track settlement, further increasing train-track dynamic interaction forces. As demonstrated in [9], at high speeds, track degradation is faster for ballasted tracks than for slab-based solutions. Therefore, the design of the underlying track system may markedly impact turnout degradation [5], safety and serviceability.

Within this context, the present study therefore aims to investigate and compare the dynamic performance of two possible track substructure solutions, namely ballasted and ballastless slab track, for a high-speed turnout with movable-point frog. The focus on movable-point turnouts is particularly relevant for high-speed railway lines, where this type of turnout is commonly adopted to ensure smoother wheel–rail transitions and improved running safety. Despite their practical importance, however, movable-point turnouts have received a relatively limited attention in the literature, especially with respect to the influence of the underlying track structure on their dynamic response.

To this end, detailed three-dimensional train-track dynamic interaction is simulated in the time domain using a non-commercial software, called ADTreS [4, 10, 11], developed at the Department of Mechanical Engineering of Politecnico di Milano. The rail vehicle is modelled with a multi-body approach, while the track system is schematised using the finite element (FE) method [4, 5]. This modelling choice allows the structural flexibility and spatial variability of the turnout to be explicitly represented, whereas in railway vehicle dynamics simulations the track is often simplified by means of a co-running track model, as also adopted in benchmark studies such as that proposed by Bezin et al. [12, 13].

The wheel–rail contact is modelled using a multi-Hertzian formulation, allowing for multiple simultaneous contact points as the wheel transitions between different rails in the turnout. The formulation accounts for the spatial variability of rail geometry along the turnout and for the possibility of multiple contacts with elements having different stiffness, ensuring an accurate representation of impact phenomena [5]. The equations of motion of the vehicle and the track are integrated simultaneously within the same simulation environment, without the need for co-simulation between separate solvers. This distinguishes the present approach from methods in which the multi-body vehicle dynamics and the track structural response are handled by separate software packages coupled iteratively [14], as well as from formulations based on moving Green's functions [15], which offer computational efficiency but are limited to linearised models of the vehicle and the track. As sample results, rail and sleeper accelerations are presented at selected cross-sections of the turnout as indicators of the dynamic stress state of the structural components, together with the vertical forces transmitted to the ground, which represent the primary excitation source for ground-borne vibration propagation analyses.

The remaining part of this work is organised as follows. Section 2 provides a detailed description of the FE models of the turnout for both track configurations. Section 3 presents and

critically discusses the results of the simulations. Finally, Section 4 draws the main conclusions, summarising the key findings and limitations of this preliminary study and identifying directions for future work. The main model parameters are reported in APPENDIX A.

2 TIME DOMAIN MODEL OF TRAIN-TRACK DYNAMIC INTERACTION

This section is devoted to the presentation of the models employed in this study. The reader is first provided with a description of the software adopted to simulate train-track dynamic interaction in the time domain, namely ADTreS [10, 11]. Attention is then turned to illustrating the geometry and the main features of the High-Speed Railway (HSR) movable-point turnout investigated in this work, for both ballasted and slab track configurations.

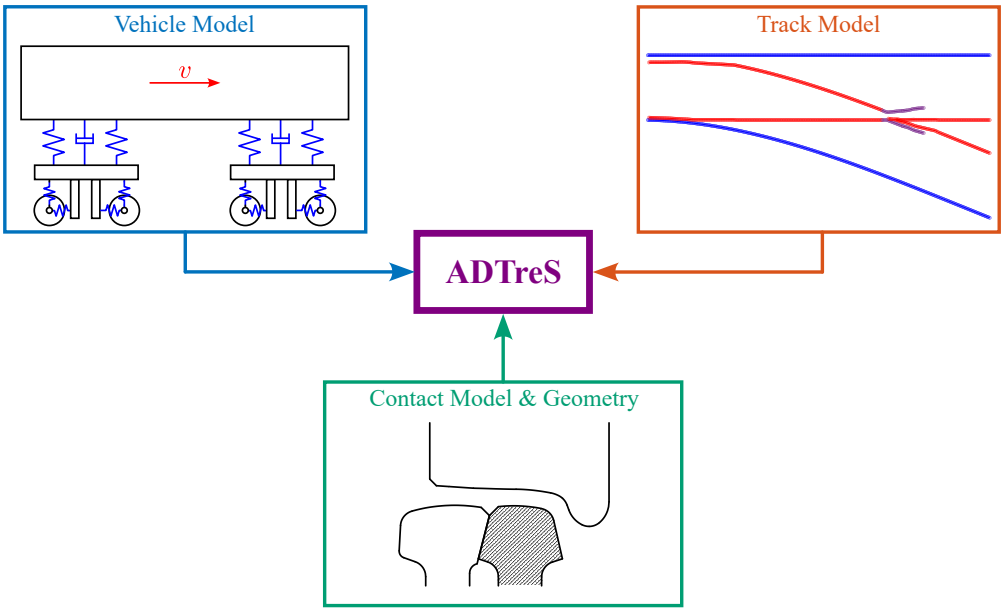


Figure 1: The ADTreS simulation environment.

The ADTreS software allows the simulation of train-track dynamic interaction in the time domain. The structure of the ADTreS simulation environment is schematised in Figure 1. The trainset, modelled with a multi-body approach, and the track structure, modelled via the finite element method (see Sections 2.1 and 2.2), are two separate subsystems whose equations of motion are coupled through contact forces.

The vehicle is represented by an assembly of rigid and flexible bodies, including carbodies, bogies and wheelsets, connected through primary and secondary suspensions [10]. Specifically, carbodies and bogies are treated as rigid bodies, while wheelsets are modelled using a modal superposition approach as deformable bodies, so as to capture their high-frequency dynamics [4, 10].

Wheel-rail contact forces are defined by a multi-Hertzian formulation [16, 17], which allows reproducing the simultaneous occurrence of multiple contact points between each wheel and the different rails of the turnout [5]. A preliminary geometric analysis is performed to identify potential contact locations and to store the corresponding parameters in a look-up table as a function of the lateral relative displacement and yaw angle of the wheelset, accounting for the spatial variability of rail profiles along the turnout. During simulation, contact kinematics are evaluated to determine active contact points; normal forces are then calculated using Hertzian theory, while tangential forces are obtained, considering the Shen-Hedrick-Elkins formulation

[18], as a function of normal load and relative creepages. The contributions from all active contacts are combined and projected onto the corresponding degrees of freedom to obtain the generalised forces acting on both the trainset and the track [10].

The coupled train-track equations of motion are solved in the time domain, using a modified Newmark integration approach. In particular, due to the non-linear nature of wheel-rail contact, an iterative procedure is carried out within each time-step of the simulation, until convergence on contact forces is achieved [19]. For a detailed description of ADTreS software, please refer to [5, 11, 19, 20].

2.1 Turnout on Ballasted Track

The HSR turnout considered in the analysis is a movable-point turnout installed on ballast, with a crossing-angle tangent of 0.022. The maximum allowed speed is 160 km/h on the diverging route and 300 km/h on the main route.

The layout of the turnout is shown in Figure 2. The rails are fastened to concrete sleepers spaced at 0.6 m, apart from some exceptions in the switch and crossing zones. The turnout extends over 242 sleepers, corresponding to a total length of about 145 m. Along the turnout, the rails of both the main route and the diverging route are fastened to the same sleepers. Thus, referring to the reference system shown in Figure 2, the sleeper length ranges from 2.6 m at the beginning of the turnout to 4.6 m at the exit section.

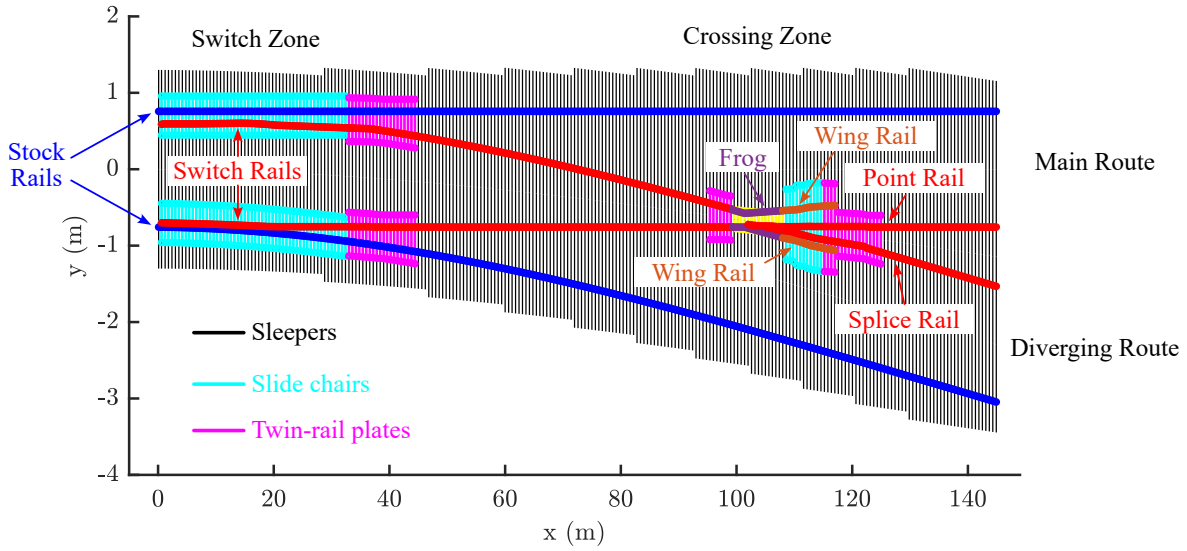
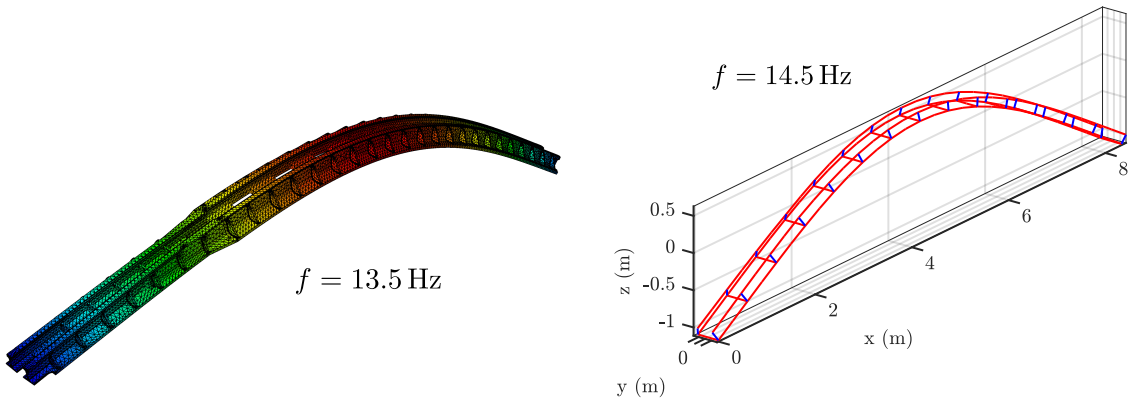


Figure 2: Adopted layout for the HSR movable-point turnout (top-view).

The track structure is included in ADTreS using the finite element method. Rather than reproducing the detailed geometry of each component through solid elements, an equivalent beam-and-lumped-mass representation was adopted to reduce the number of degrees of freedom and the associated computational cost, similarly to what was proposed in [21]. Precisely, the rails are modelled using Euler-Bernoulli beam elements. For the switch rails, point rails, and splice rails, whose cross-sections vary along the turnout, the properties of the different cross-sections were extracted from CAD software by considering the actual geometry. The same cross-sections are used to generate the look-up tables adopted to identify the wheel-rail contact points.

While the approximation of the rails as Euler-Bernoulli beams is fully appropriate, the same assumption is less straightforward for the frog, which is manufactured as a single cast component



(a) (b)

Figure 3: First bending mode of the frog. (a) FE model (f=13.5 Hz) in a commercial software; (b) equivalent beam model (f=14.5 Hz).

with a complex geometry, as shown in Figure 3a. In this case, a modal analysis of the component considering its actual geometry is first performed in a commercial FE software, excluding the wing rails. Then, an equivalent beam model is developed so as to reproduce the same inertial properties and the same natural frequency associated with the first bending mode (shown in Figure 3a). The resulting equivalent beam model is reported in Figure 3b. Three different types of cross-sections were considered in the construction of this portion of the model. Specifically, one for the zone where the train wheel passes, one for the lower part, and one for the transverse connections between the two wings of the frog. The nodes of the upper and lower beams are connected through rigid Multi-Point Constraints (MPCs), which simulate the ribs. The actual frog has a first bending natural frequency of 13.5 Hz, whereas the corresponding value obtained with the equivalent beam model is 14.5 Hz.

The sleepers, as the rails, are modelled using Euler-Bernoulli beam elements. Each sleeper is discretised with a number of elements that varies according to its position along the turnout. Except at the sleeper ends and at the midpoint, nodes are introduced at each rail seat location. The fastening systems connecting the rails to the sleepers are modelled differently depending on their type. The standard single fastenings, which are not shown in Figure 2, are modelled as lumped masses of 8.7 kg connected to the corresponding sleeper node through MPCs, whereas the railpads are modelled as lumped viscoelastic elements with a vertical stiffness of 450 MN/m.

The slide chairs and twin-rail plates, shown in cyan and magenta respectively in Figure 2, are modelled as beam elements, so as to take their flexibility into account. At the slide chairs, both in the switch zone and in the crossing zone, the rigid connection between the slide chairs and the stock rails (switch zone) and wing rails (crossing zone) is modelled through an MPC, whilst the contact in the vertical direction between the movable rails and the plates is modelled using single-sided springs, the stiffness of which has been tuned to represent the local flexibility of the bodies in contact. The same approach is used for the contact in the lateral direction between switch rails and stock rails and between point/splice rails and wing rails. A rigid connection between the nodes was instead used for the spacers and for the screws and bolts connecting the point and splice rails. In the case of all twin-rail plates, where the rails are fixed, the respective railpads are modelled as concentrated viscoelastic elements. The elastic pads interposed between slide chairs and twin-rail plates and sleepers are modelled as elastic beds. The same applies to the elastic pads placed between the frog and the sleepers.

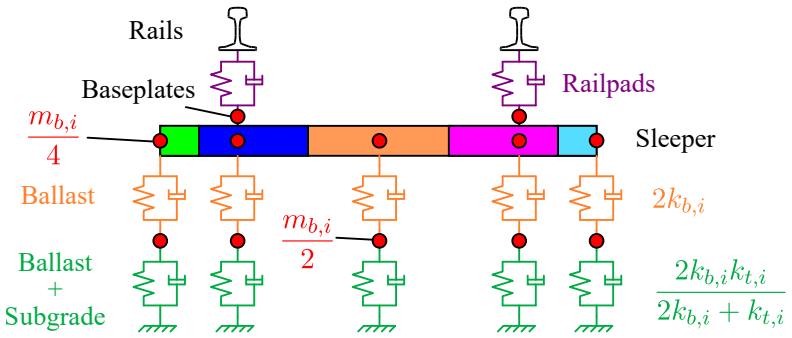


Figure 4: Cross-sectional view of ballasted track model.

The model adopted for the ballast layer below the sleepers, having a thickness of 0.35 m, and the subgrade below the ballast is schematised in Figure 4. This model is based on the work by Zhai et al. in [22] and allows the inclusion of both the stiffness effect and the inertial effect of the ballast layer. It is modelled as concentrated spring–mass–spring systems acting at each sleeper node. The stiffness and dashpot coefficients of each viscoelastic element are computed from the stiffness and damping per unit surface of the ballast and the subgrade. Considering the vertical direction, they are equal to 133 MN/m/m^2 and 27.8 kNs/m/m^2 for the ballast and 267 MN/m/m^2 and 88.9 kNs/m/m^2 for the subgrade. The conversion to concentrated stiffness and dashpot coefficients is then obtained by considering the area of the sleeper covered by each element, indicated with different colours in Figure 4.

The same is done with the mass of the ballast, computed considering a density equal to 1800 kg/m^3. The 25% of the ballast mass is assigned to the sleeper nodes, the 50% to nodes positioned at mid-height of the ballast layer, while the remaining 25% is assumed not to participate in the ballast vibration. The stiffness coefficients of the two stiffness layers are then obtained by considering the stiffness of the ballast and the subgrade in series. Denoting by $K_{b,i}$ and $K_{t,i}$ the resulting stiffnesses of ballast and subgrade associated with the i-th element, respectively, the stiffness of the two layers can be obtained as follows:

$$K_{1,i} = 2K_{b,i} \tag{1a}$$

$$K_{2,i} = \frac{2K_{b,i}K_{t,i}}{2K_{b,i} + K_{t,i}} \tag{1b}$$

The layout of the turnout from the FE module implemented in the ADTreS simulation environment in correspondence of short sections of the switch and crossing zones is shown in Figures 5a and 5b, respectively. The beam elements are shown in red, concentrated masses as blue dots, MPCs as blue thin lines, and viscoelastic elements as black and magenta lines. Instead, elastic beds are not visualised. The main mechanical parameters of the FE model are reported in Table A1.

2.2 Turnout on Slab Track

As HSR turnouts in Italy are all installed on ballast and those on slab track are still the subject of ongoing research, some assumptions are made in designing the slab track turnout. The same components as in the ballasted turnout are considered, including the sleepers, which are fixed to the slabs through Under-Sleeper Pads (USPs). These elements are not present in the ballasted track model. The layout of the slabs considered in the analysis is shown in Figure 6,

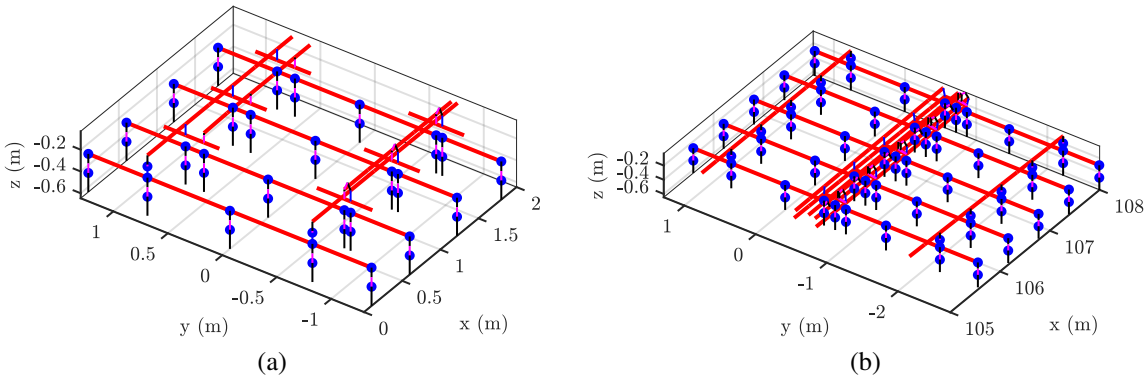


Figure 5: Details of the FE model of the turnout on ballasted track. (a) Switch zone; (b) crossing zone.

where different colours outline regions characterised by slabs of different width. Pre-fabricated concrete slabs are assumed, each accommodating six sleepers. A 4 cm gap is left between adjacent slabs, with no coupling between them, in order to avoid issues associated with thermal deformations due to temperature variations throughout the year [23]. Three different slab widths are used equal to 3.3 m, 4.1 m and 5.2 m, indicated in blue, red and green in Figure 6, respectively, in order to limit the number of formworks required for manufacturing. The slabs are modelled using Kirchhoff-Love plate finite elements.

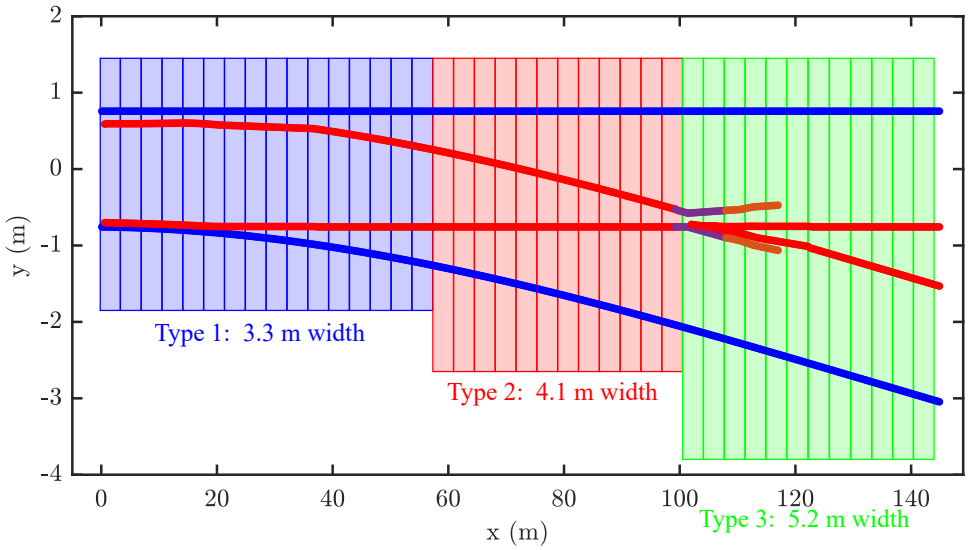


Figure 6: Turnout on slab track.

The general cross-section of the ballastless track is shown in Figure 7. All the slabs have a thickness of 0.2 m. The slabs are connected to a concrete foundation of 0.3 m thickness through a mortar layer of 2 cm, that is modelled as an elastic bed. The stiffness of the elastic bed is computed considering a mortar Young's modulus of 45 GPa. As for the slabs, the foundation layer is modelled using Kirchhoff-Love plate finite elements.

The elastic layers, associated with the USPs and the subgrade below the foundation, are modelled as lumped viscoelastic elements, applied at the same locations as those used in the ballasted track model, so as to allow a direct comparison between the two turnout configurations. The same stiffness and damping coefficients per unit surface are adopted for the subgrade, while

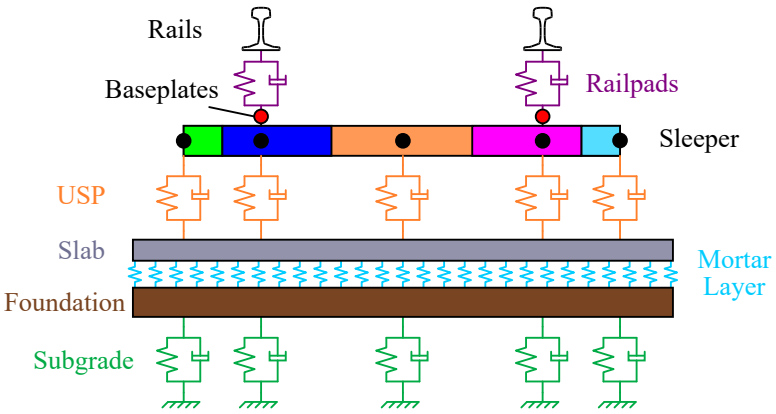


Figure 7: Cross-sectional view of slab track model.

those of each viscoelastic element are computed considering the foundation surface area on which they act. The stiffness and damping coefficients of the elements representing the USPs are computed in the same way as those representing the ballast in the ballasted turnout, i.e. starting from values per unit surface and considering the area of the lower face of the sleeper. The stiffness per unit surface of the USP is tuned so as to limit the rail deflection to 1 mm under an axle load of 150 kN. The tuning is carried out using the simplified analytical model of the slab track shown in Figure 8, which describes the vertical dynamics of a straight track with the same design. The rails, the slab and the foundation are modelled as Euler–Bernoulli beams, with the sleeper mass continuously distributed. The USP, the mortar layer and the subgrade are modelled as continuous elastic layers.

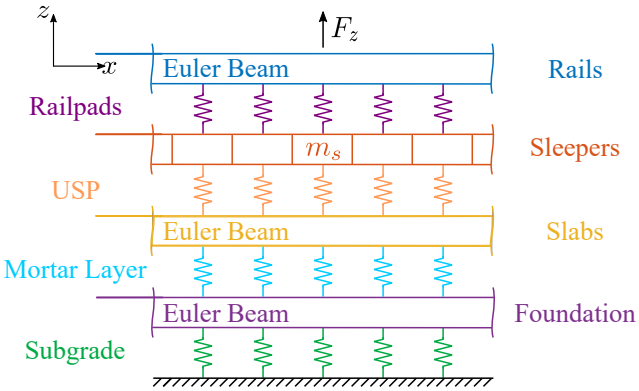


Figure 8: Simplified analytical model of the slab track.

Based on a static analysis with an axle load of 150 kN applied at coordinate x=0, the stiffness per unit surface of the USP elastic layer is set to 80 MN/m/m^2. The resulting rail displacement distribution as a function of position is shown in Figure 9a, in which the maximum displacement is kept slightly below the 1 mm limit.

The damping coefficient is instead determined from a frequency domain dynamic analysis using the same model, by imposing a loss factor η=0.25 and computing the equivalent viscous damping at the cut-on frequency of the bending wave in the rails. The Frequency Response Functions (FRFs) between the accelerations of the different layers due to a unit force applied to the rails are shown in Figure 9b. The cut-on frequency of the bending wave is approximately 55 Hz, yielding a damping coefficient per unit surface of 58 kNs/m/m^2. The additional parameters of the FE model of the ballastless turnout are collected in Table A2.

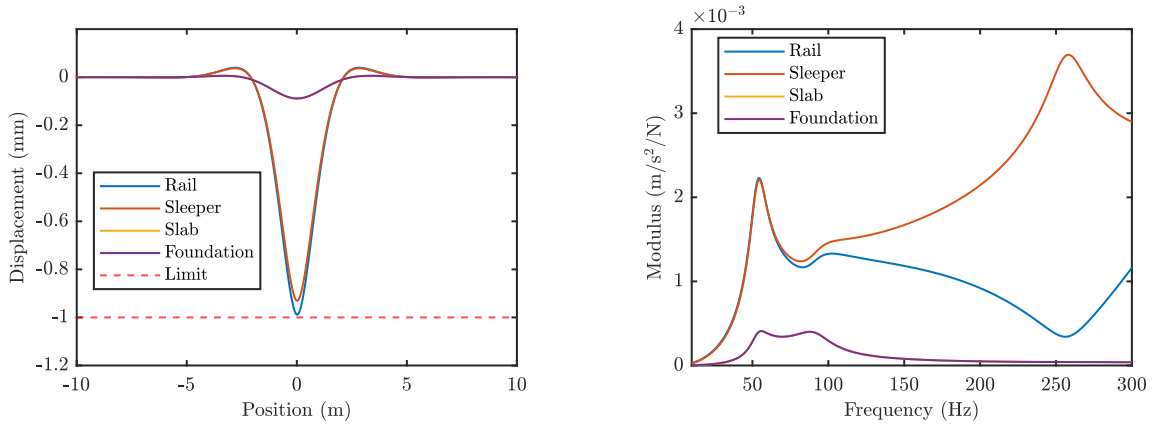


Figure 9: Results of the simplified model of the turnout on slabs. (a) Static deflection under a 150 kN force at x=0; (b) Vertical point accelerances due to a force applied to the railhead.

The stiffness of the USP controls the static rail deflection under the axle load. The stiffer the USP, the lower the rail deflection. Dynamically, the stiffness of the USP governs the transmission of dynamic forces to the slab: a softer layer improves the vibration isolation of the slab and the foundation, reducing the transmitted forces, and hence the ground-borne vibrations, along with enhanced subgrade preservation. On the other hand, a softer USP increases the accelerations of the sleepers, and therefore the dynamic loading of sleeper-mounted components such as the switch actuation devices of the turnout.

The damping coefficient mainly controls the amplitude of the response at the track resonance frequencies, reducing the resonance peaks. By dissipating part of the vibrational energy, it also contributes to limiting the transmission of vibration to the supporting structure, thereby reducing ground-borne vibration levels within the corresponding frequency range.

3 RESULTS

This section presents and discusses a set of preliminary results from simulations carried out on the ballasted and ballastless turnouts. The analysis considers a high-speed passenger train travelling through the turnout in the facing move direction along the main route at a speed of 300 km/h, kept constant throughout the simulation. The main route is extended before and after the turnout; in these extension sections, sleepers of 2.6 m length are adopted, and, in the case of ballastless track, slabs of 2.7 m width. A rail irregularity profile is applied to both rails: for wavelengths in the D1 range (3-25 m), longitudinal levels and lateral alignments measured by a diagnostic train are adopted, while for shorter wavelengths a spatial realisation of the PSD of the rail roughness prescribed by the EN 13979 Standard is summed to the longitudinal level [24].

For the sake of clarity and conciseness, three specific cross-sections are considered: the first is located 6 m before the start of the turnout, the second at its entrance, and the third 3.6 m after it. Results are presented in terms of vertical accelerations evaluated at structural nodes and of vertical forces transmitted to the ground during train passage. All data are low-pass filtered at 300 Hz. The vertical accelerations of the left and right rails at the section located 6 m before the turnout entrance are shown in Figures 10a and 10b, respectively: on the upper part, time histories are plotted, while the bottom part of the figure reports their spectra. It is possible to observe that acceleration time histories exhibit comparable magnitudes, well below 30 m/s^2.

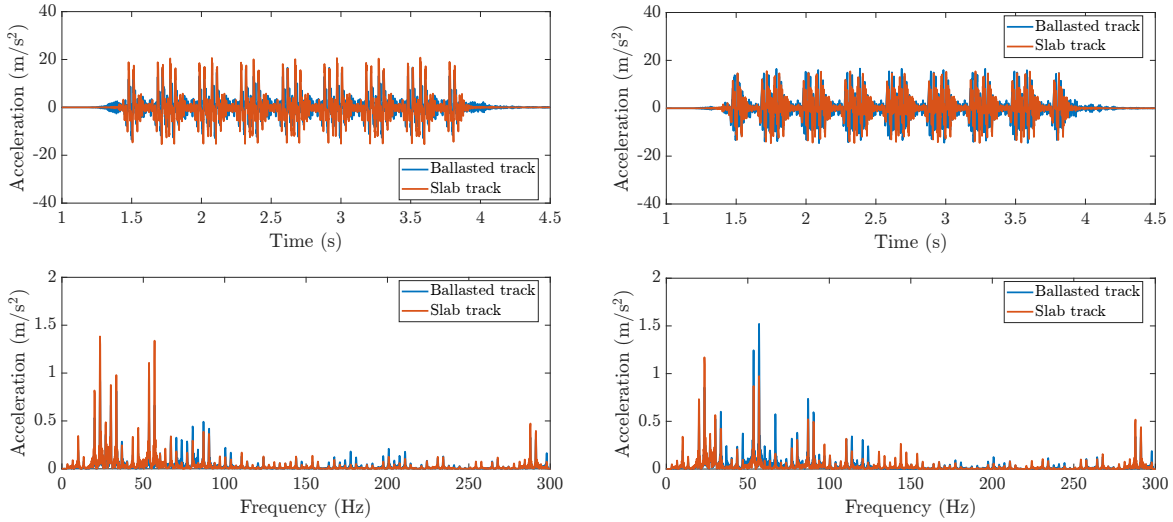


Figure 10: Rail vertical accelerations 6 m before the starting section of the turnout. Upper plot: time history. Lower plot: spectrum. (a) Left rail and (b) right rail with respect to the travelling direction.

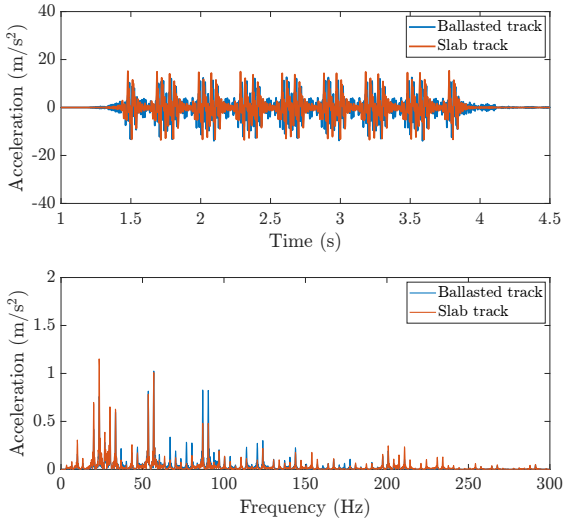


Figure 11: Sleeper vertical acceleration at midspan, 6 m before the starting section of the turnout. Upper plot: time history. Lower plot: spectrum.

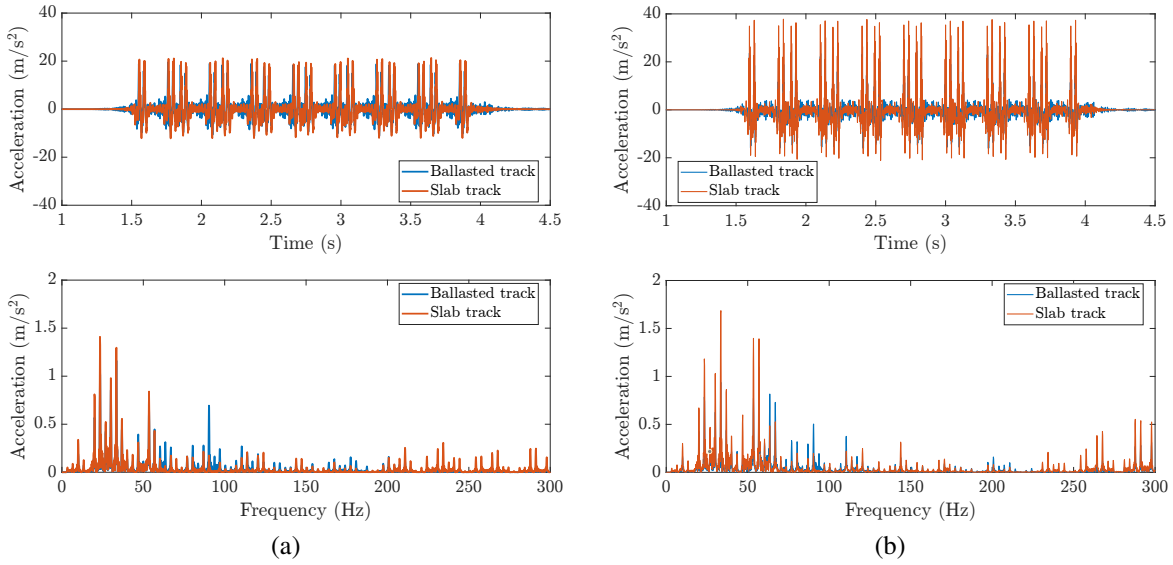


Figure 12: Sleeper vertical acceleration at midspan. Upper plot: time history. Lower plot: spectrum. (a) At the starting section of the turnout; (b) 3.6 m after the starting section.

Figure 11 shows the sleeper midspan vertical accelerations at the same cross-section, together with their spectra. Consistently with the observations at rail level, the two track solutions yield comparable acceleration magnitudes at sleeper level.

Subsequently, Figure 12 extends the comparison to two additional sections: the first located at the turnout entrance (Figure 12a), and the other located 3.6 m after the entrance (Figure 12b). Although acceleration peak amplitudes remain comparable between the two configurations at the turnout entrance (with a variation about 10%), more pronounced differences are observed 3.6 m downstream of the starting section: in particular, larger sleeper midspan acceleration is obtained for the slab track configuration.

While sleeper accelerations provide an indication of the dynamic stress state of the switch components, another relevant indicator is the vertical force transmitted to the ground by the track structure, which is directly related to both the magnitude and the rate of subgrade degradation over time induced by train passage. To this end, Figure 13 shows the total vertical force transmitted to the ground at the three analysed cross-sections for both the ballasted and slab track configurations. A substantial reduction in the forces transmitted to the ground can be observed when moving from the ballasted track configuration (blue curve) to the slab track solution (orange curve): this is due to the fact that the slab track configuration yields a more uniform distribution of the loads transmitted to the subgrade compared to the ballasted case.

Finally, Figure 14 summarises the results presented so far in terms of sleeper vertical accelerations and ground-transmitted forces at the three sections of interest for both track configurations. In particular, Figure 14a provides a section-by-section comparison of the RMS and peak values of the sleeper midspan accelerations for the two track configurations. The RMS values are reported in the upper panel, whereas the corresponding peak values are presented in the lower panel. As previously discussed, the most pronounced differences occur at the third section, located 3.6 m downstream of the turnout entrance: at this location, the RMS and peak acceleration values increase by 41.6% and 53.2% respectively, moving from ballasted to slab track. For the specific parameter calibration adopted in the two models, the slab track configuration consistently exhibits higher RMS and peak acceleration values.

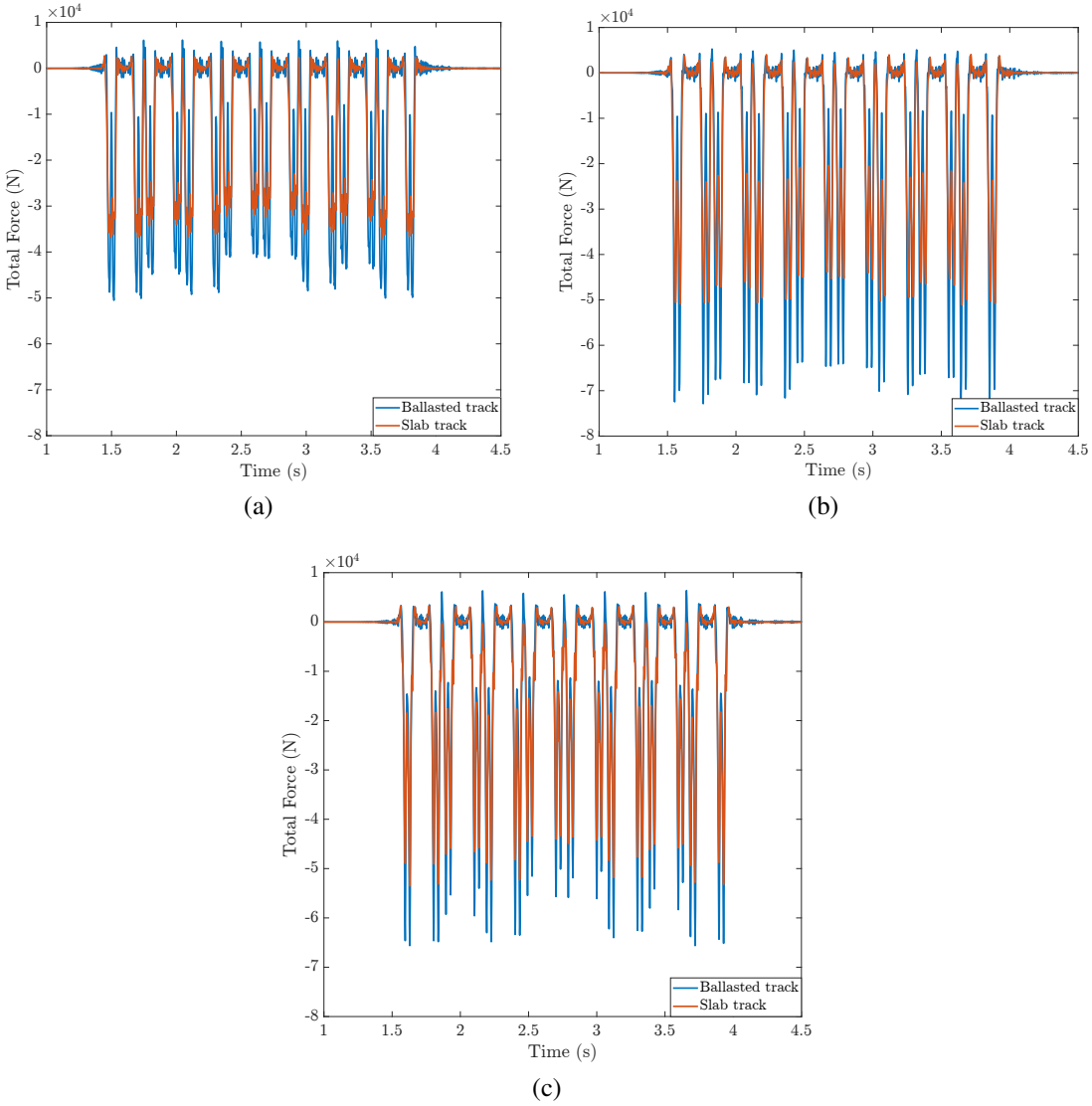
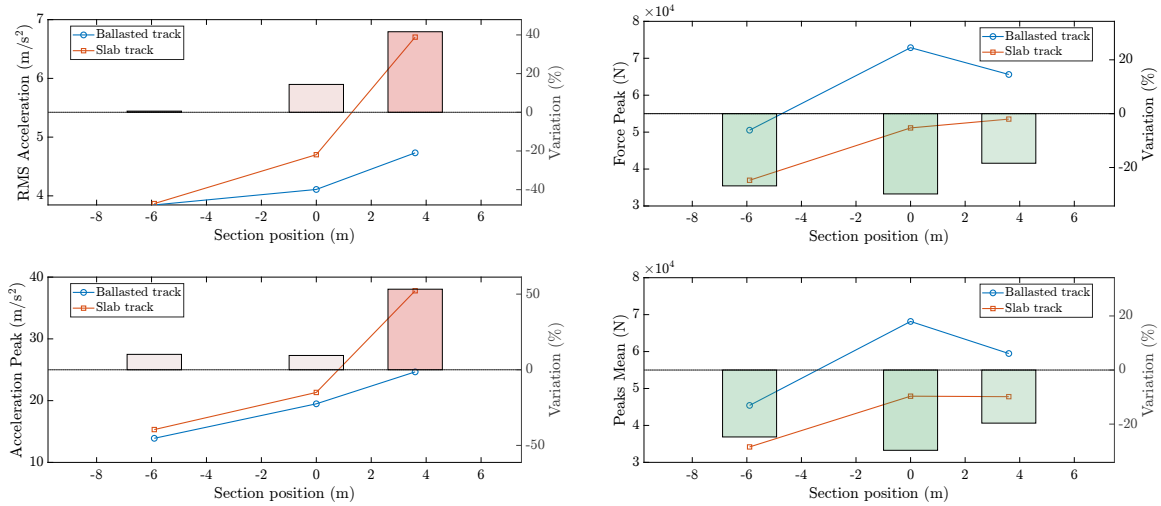


Figure 13: Total cross-sectional vertical force transmitted to the ground. (a) 6 m before the starting section of the turnout; (b) at the starting section; (c) 3.6 m after the starting section.

Instead, Figure 14b quantitatively compares the forces transmitted to the ground in the two configurations. Specifically, the upper part shows the maximum total force values, while the lower panel reports the mean axle-by-axle peak forces. It can be observed that the slab track configuration is beneficial in terms of total ground-transmitted force, yielding a maximum reduction of 29.8% in its peak value.

Although the results obtained in this work are inherently dependent on the parameters adopted for the two track models (see Sections 2.1-2.2), a key aspect clearly emerges from the analyses. As expected, the advantage associated with the slab track solution lies in the more uniform distribution of the forces transmitted to the supporting ground during train passage. In particular, local force peaks appear less pronounced compared with the ballasted configuration, leading to a smoother stress distribution within the supporting layers. The reduced localisation of contact forces provided by the slab track system may result in beneficial effects in terms of subgrade preservation and long-term maintenance performance [25], as well as in mitigating ground-borne vibrations generated by the train-track interaction [26].



(a) (b)

Figure 14: Quantitative comparison between ballasted and slab track configurations, considering three distinct sections. (a) RMS values of sleeper midspan vertical accelerations (upper part) and acceleration peak values (lower part); (b) Maximum total force values (upper part) and the mean axle-by-axle peak forces (lower part). Bars represent variations occurring when moving from a ballasted to a slab track configuration.

4 CONCLUSIONS

This work presents a preliminary comparative investigation of the dynamic behaviour of ballasted and slab track solutions for a high-speed movable-point turnout. To this end, a detailed three-dimensional train–track dynamic interaction model was developed within the ADTreS simulation environment, accounting for the spatial variability of rail profiles along the turnout [4] and for the possibility of multiple simultaneous wheel–rail contact points. Two alternative track substructure configurations were considered: a conventional ballasted track and a ballastless solution based on pre-fabricated concrete slabs.

Numerical analyses focused on comparing the two track solutions in terms of rail and sleeper accelerations, as well as the dynamic forces transmitted to the supporting ground during train passage at 300 km/h. The results indicate that, for the three analysed sections, the slab track configuration consistently produces higher sleeper midspan acceleration levels than the ballasted track. The most remarkable differences are observed 3.6 m after the beginning of the turnout, where the RMS and peak acceleration values increase by approximately 41.6% and 53.2%, respectively.

Conversely, the slab track configuration provides a significant benefit in terms of the forces transmitted to the ground. Owing to a more uniform distribution of the dynamic loads induced by train passage, the ballastless configuration considerably reduces force peaks compared with the ballasted solution. Depending on the analysed cross-section, the reduction in terms of peak transmitted force reaches 29.8%. This is particularly relevant in view of the well-established relationship between concentrated dynamic loads and the degradation of ballast and subgrade layers. The slab track solution may therefore provide beneficial effects in terms of subgrade preservation, mitigation of differential settlements and reduced long-term maintenance requirements.

It should be emphasised, however, that the results presented here are inherently dependent

on the modelling assumptions adopted for the two track configurations (see Sections 2.1–2.2), particularly concerning the stiffness and damping properties of the supporting layers and the tuning of the Under-Sleeper Pad (USP) parameters. Furthermore, the present investigation is limited to a small number of turnout cross-sections and to a single operating condition in terms of train typology and speed. For these reasons, the results should be regarded as preliminary, yet representative of the different dynamic behaviour characterising the two track solutions. Future developments will include a broader parametric investigation of both configurations, together with experimental validation activities.

REFERENCES

[1] Pegah Barkhordari and Roberto Galeazzi. "Statistical Model of Railway's Turnout based on Train Induced Vibrations". In: *IFAC-PapersOnLine* 51.24 (2018), pp. 1278–1284. DOI: 10.1016/j.ifacol.2018.09.570.

[2] Gunnstein T. Frøseth and Anders Rönnquist. "Evolution of load conditions in the Norwegian railway network and imprecision of historic railway load data". In: *Structure and Infrastructure Engineering* 15.2 (2018), pp. 152–169. DOI: 10.1080/15732479.2018.1504087.

[3] Guoqing Jing, Mohammad Siahkouhi, Kun Qian, and Shuguo Wang. "Development of a field condition monitoring system in high speed railway turnout". In: *Measurement* 169 (2021), p. 108358. DOI: 10.1016/j.measurement.2020.108358.

[4] S. Alfi and S. Bruni. "Mathematical modelling of train–turnout interaction". In: *Vehicle System Dynamics* 47.5 (2009), pp. 551–574. DOI: 10.1080/00423110802245015.

[5] S. Bruni, I. Anastasopoulos, S. Alfi, A. Van Leuven, and G. Gazetas. "Effects of train impacts on urban turnouts: Modelling and validation through measurements". In: *Journal of Sound and Vibration* 324.3-5 (2009), pp. 666–689. DOI: 10.1016/j.jsv.2009.02.016.

[6] V.L. Markine and I. Shevtsov. "Experimental Analysis of the Dynamic Behaviour of Railway Turnouts". In: *Proceedings of the Eleventh International Conference on Computational Structures Technology*. Vol. 99. CST2012. Civil-Comp Press, 2012. DOI: 10.4203/ccp.99.131.

[7] Sakdirat Kaewunruen. "Monitoring structural deterioration of railway turnout systems via dynamic wheel/rail interaction". In: *Case Studies in Nondestructive Testing and Evaluation* 1 (2014), pp. 19–24. DOI: 10.1016/j.csndt.2014.03.004.

[8] Björn A. Pålsson and Jens C.O. Nielsen. "Wheel–rail interaction and damage in switches and crossings". In: *Vehicle System Dynamics* 50.1 (2012), pp. 43–58. DOI: 10.1080/00423114.2011.560673.

[9] C. Charoenwong, D.P. Connolly, A. Colaço, P. Alves Costa, P.K. Woodward, A. Romero, and P. Galvín. "Railway slab vs ballasted track: A comparison of track geometry degradation". In: *Construction and Building Materials* 378 (2023), p. 131121. DOI: 10.1016/j.conbuildmat.2023.131121.

[10] Egidio Di Gialleonardo, Francesco Braghin, and Stefano Bruni. "The influence of track modelling options on the simulation of rail vehicle dynamics". In: *Journal of Sound and Vibration* 331.19 (2012), pp. 4246–4258. DOI: 10.1016/j.jsv.2012.04.024.

[11] S Bruni, A Collina, R Corradi, and G Diana. "Numerical simulation of train-track-bridge dynamic interaction". In: *COMPUTATIONAL MECHANICS, PROCEEDINGS*. Ed. by ZH Yao, MW Yuan, and WX Zhong. 6th World Congress on Computational Mechanics held in conjunction with the 2nd Asian-Pacific Congress on Computational Mechanics, Beijing, China, SEP 05-10, 2004. TSINGHUA UNIV PRESS, 2004, pp. 237–242.

[12] Yann Bezin and Björn A. Pålsson. "Multibody simulation benchmark for dynamic vehicle-track interaction in switches and crossings: modelling description and simulation tasks". In: *Vehicle System Dynamics* 61.3 (2023), pp. 644–659. DOI: 10.1080/00423114.2021.1942079.

[13] Y. Bezin, B.A. Pålsson, W. Kik, P. Schreiber, J. Clarke, V. Beuter, M. Sebes, I. Persson, H. Magalhaes, P. Wang, and P. Klauser. "Multibody simulation benchmark for dynamic vehicle–track interaction in switches and crossings: results and method statements". In: *Vehicle System Dynamics* 61.3 (2023), pp. 660–697. DOI: 10.1080/00423114.2021.1959038.

[14] Anders Johansson, Björn Pålsson, Magnus Ekh, Jens C.O. Nielsen, Mats K.A. Ander, Jim Brouzoulis, and Elias Kassa. "Simulation of wheel–rail contact and damage in switches & crossings". In: *Wear* 271.1-2 (2011), pp. 472–481. DOI: 10.1016/j.wear.2010.10.014.

[15] X. Li, P.T. Torstensson, and J.C.O. Nielsen. "Simulation of vertical dynamic vehicle–track interaction in a railway crossing using Green's functions". In: *Journal of Sound and Vibration* 410 (2017), pp. 318–329. DOI: 10.1016/j.jsv.2017.08.037.

[16] J. P. Pascal and G. Sauvage. "New method for reducing the multicontact wheel/rail problem to one equivalent contact patch". In: *Vehicle System Dynamics* 20.sup1 (1992), pp. 475–489. DOI: 10.1080/00423119208969417.

[17] J. Piotrowski and H. Chollet. "Wheel–rail contact models for vehicle system dynamics including multi-point contact". In: *Vehicle System Dynamics* 43.6-7 (2005), pp. 455–483. DOI: 10.1080/00423110500141144.

[18] Z. Y. SHEN, J. K. HEDRICK, and J. A. ELKINS. "A Comparison of Alternative Creep Force Models for Rail Vehicle Dynamic Analysis". In: *Vehicle System Dynamics* 12.1-3 (1983), pp. 79–83. DOI: 10.1080/00423118308968725.

[19] Lorenzo Bernardini, Francesco Morgan Bono, and Andrea Collina. "Drive-by damage detection and localization exploiting continuous wavelet transform and multiple sparse autoencoders". In: *Railway Engineering Science* 33.4 (2025), pp. 721–745. DOI: 10.1007/s40534-025-00393-5.

[20] Francesco Braghin, Stefano Bruni, and Giorgio Diana. "Experimental and numerical investigation on the derailment of a railway wheelset with solid axle". In: *Vehicle System Dynamics* 44.4 (2006), pp. 305–325. DOI: 10.1080/00423110500337494.

[21] C. Somaschini, Q. Li, S. Alfi, E. Di Gialleonardo, and A. Collina. "Validation of a movable-point turnout design: a complete vehicle-turnout interaction model". In: *Proceedings of the Sixth International Conference on Railway Technology: Research, Development and Maintenance*. Ed. by J. Pombo. Vol. 7. Civil-Comp Conferences. Online volume: CCC 7, Paper 6.16. Edinburgh, UK: Civil-Comp Press, 2024. DOI: 10.4203/ccc.7.6.16.

[22] W.M. Zhai, K.Y. Wang, and J.H. Lin. "Modelling and experiment of railway ballast vibrations". In: *Journal of Sound and Vibration* 270.4-5 (2004), pp. 673–683. DOI: 10.1016/s0022-460x(03)00186-x.

[23] Qian Zhang, Xiaopei Cai, Yanglong Zhong, Zelin Chen, and Changchang Wang. "Temperature field and thermal effects of the longitudinal connected slab track based on the measurement data and thermal-fluid-structure coupling analysis". In: *Construction and Building Materials* 343 (2022), p. 128121. DOI: 10.1016/j.conbuildmat.2022.128121.

[24] European Committee for Standardization (CEN). *Railway applications – Wheelsets and bogies – Monobloc Wheels – Technical approval procedure – Part 1: Forged and rolled wheels*. EN 13979-1:2023. European Standard. 2023.

[25] Ilaria Grossoni, William Powrie, Antonis Zervos, Yann Bezin, and Louis Le Pen. "Modelling railway ballasted track settlement in vehicle-track interaction analysis". In: *Transportation Geotechnics* 26 (2021), p. 100433. DOI: 10.1016/j.trgeo.2020.100433.

[26] Federico Castellini, Leonardo Faccini, and Andrea Collina. "On the vibration induced by train operations in tunnels: a comparative study of different track systems through experiments and numerical simulations". In: *International Journal of Rail Transportation* 14.1 (2025), pp. 136–152. DOI: 10.1080/23248378.2025.2486470.

[27] European Committee for Standardization (CEN). *Railway applications - Track - Rail - Part 1: Track rails*. EN 13674-1:2011. European Standard. 2011.

APPENDIX A TRACK MODEL PARAMETERS

The main parameters of the FE model of the turnout on ballasted track are reported in Table A1.

Rails	
Parameter	Value
Rail type	60E1 [27]
Young's modulus	206 GPa
Poisson ratio	0.3
Railpads	
Parameter	Value
Vertical stiffness	450 MN/m
In-plane stiffness	225 MN/m
Vertical damping	4.5 kNs/m
In-plane damping	2.25 kNs/m
Slide chairs/Twin-rail baseplate pads	
Parameter	Value
Vertical stiffness (unit surface)	13.3E+03 MN/m^3
Shear stiffness (unit surface)	6.7E+03 MN/m^3
Vertical damping (unit surface)	133 kNs/m^3
Shear damping (unit surface)	66.7 kNs/m^3
Sleepers	
Parameter	Value
Density	2500 kg/m^3
Young's modulus	35 GPa
Poisson ratio	0.25
Cross-sectional area	0.30x0.18 m^2
Ballast	
Parameter	Value
Density	1800 kg/m^3
Vertical stiffness (unit surface)	133 MN/m^3
Shear stiffness (unit surface)	67 MN/m^3
Vertical damping (unit surface)	27.8 kNs/m^3
Shear damping (unit surface)	13.9 kNs/m^3
Subgrade	
Parameter	Value
Vertical stiffness (unit surface)	267 MN/m^3
Shear stiffness (unit surface)	133 MN/m^3
Vertical damping (unit surface)	88.9 kNs/m^3
Shear damping (unit surface)	44.4 kNs/m^3

Table A1: Main parameters of the FE model of ballasted track turnout.

The additional parameters of the FE model of the ballastless turnout are listed in Table A2.

Slabs	
Parameter	Value
Density	2500 kg/m^3
Young's modulus	35 GPa
Poisson ratio	0.25
Width	3.3 m/4.1 m/5.2 m/2.7 m (straight track)
Thickness	0.2 m
Gap	0.04 m
Foundation	
Parameter	Value
Density	2500 kg/m^3
Young's modulus	35 GPa
Poisson ratio	0.25
Width	3.3 m/4.1 m/5.2 m/2.7 m (straight track)
Thickness	0.3 m
Mortar layer	
Parameter	Value
Vertical stiffness (unit surface)	225E+04 MN/m^3
Shear stiffness (unit surface)	113E+04 MN/m^3
Vertical damping (unit surface)	300E+02 kNs/m^3
Shear damping (unit surface)	120E+02 kNs/m^3

Table A2: Main parameters of the FE model of the ballastless track turnout.